Article

Long-lived zone-boundary magnons in an antiferromagnet

Jeongheon Choe [1,2,11], David Lujan[1,2,11], Gaihua Ye[3], Cynthia Nnokwe[3], Bowen Ma[1], Jiaming He [4], Frank Y. Gao [1,2], T. Nathan Nunley[1,2], Aritz Leonardo [5,6], Mikel Arruabarrena[6,7], Andres Ayuela[6,7], Jianshi Zhou[2,4], Martin Rodriguez-Vega [1,2,8] ✉, Gregory A. Fiete [8,9,10], Rui He[3] ✉ & Xiaoqin Li [1,2] ✉

Antiferromagnetic (AFM) insulators exhibit many desirable features for spintronic applications such as fast dynamics in the THz range and robustness to fluctuating external fields. However, large damping typically associated with THz magnons presents a serious challenge for THz magnonic applications. Here, we report long-lived short-wavelength zone boundary magnons in the honeycomb AFM insulator $CoTiO_3$, recently found to host topological magnons. We find that its zone-boundary THz magnons exhibit longer lifetimes than its zone-center magnons. This unusual momentum-dependent long magnon lifetime originates from several factors including the antiferromagnetic order, exchange anisotropy, a finite magnon gap, and magnon band dispersion. Our work suggests that magnon-magnon interaction may not be detrimental to magnon lifetimes and should be included in future searches for topological magnons.

Topological magnons offer an enticing solution to the outstanding challenge of damping associated with THz magnonics[1]. As newly identified bosonic excitations in crystalline magnetic insulators, topological magnons possess distinct characteristics in comparison to their electronic counterpart[1–3]. On the one hand, surface or edge states of topological magnons are protected from local defects in materials[4,5], analogous to other topological systems (e.g., electrons, acoustic phonons, and photonic crystals). On the other hand, magnons only exist as excited states and do not obey particle number conservation. Consequently, only long-lived magnons, regardless of their band topology, can offer the benefit associated with topologically protected states.

While many materials have been predicted to host topological magnons, a simple relation between magnon topology (properties of single-particle bands) and their lifetime does not exist. A prediction of the magnon lifetime must take into account magnon-magnon interactions, which necessitates theories that go beyond single-particle band descriptions[6–8]. For fermions, only electrons near the Fermi level participate in the excitation processes, allowing one to focus on low-energy Dirac cones. In contrast, bosons, unrestricted by the Pauli exclusion principle, require consideration of the entire Brillouin zone. Notably, magnons residing near the saddle points of a dispersion relation may play a particularly significant role in both electrically and optically detected magnon signals due to their high DOS. In the

[1]Department of Physics and Center for Complex Quantum Systems, The University of Texas at Austin, Austin, TX, USA. [2]Center for Dynamics and Control of Materials, The University of Texas at Austin, Austin, TX, USA. [3]Department of Electrical and Computer Engineering, Texas Tech University, Lubbock, TX, USA. [4]Department of Mechanical Engineering, The University of Texas at Austin, Austin, TX, USA. [5]EHU Quantum Center, University of the Basque Country UPV/EHU, Bilbao, Spain. [6]Donostia International Physics Center, DIPC, Donostia - San Sebastián, Spain. [7]Centro de Física de Materiales (CFM-MPC), Donostia, Spain. [8]Department of Physics, Northeastern University, Boston, MA, USA. [9]Quantum Materials and Sensing Institute, Northeastern University, Burlington, MA, USA. [10]Department of Physics, Massachusetts Institute of Technology, Cambridge, MA, USA. [11]These authors contributed equally: Jeongheon Choe, David Lujan. ✉e-mail: rodriguezvega.physics@gmail.com; rui.he@ttu.edu; elaineli@physics.utexas.edu
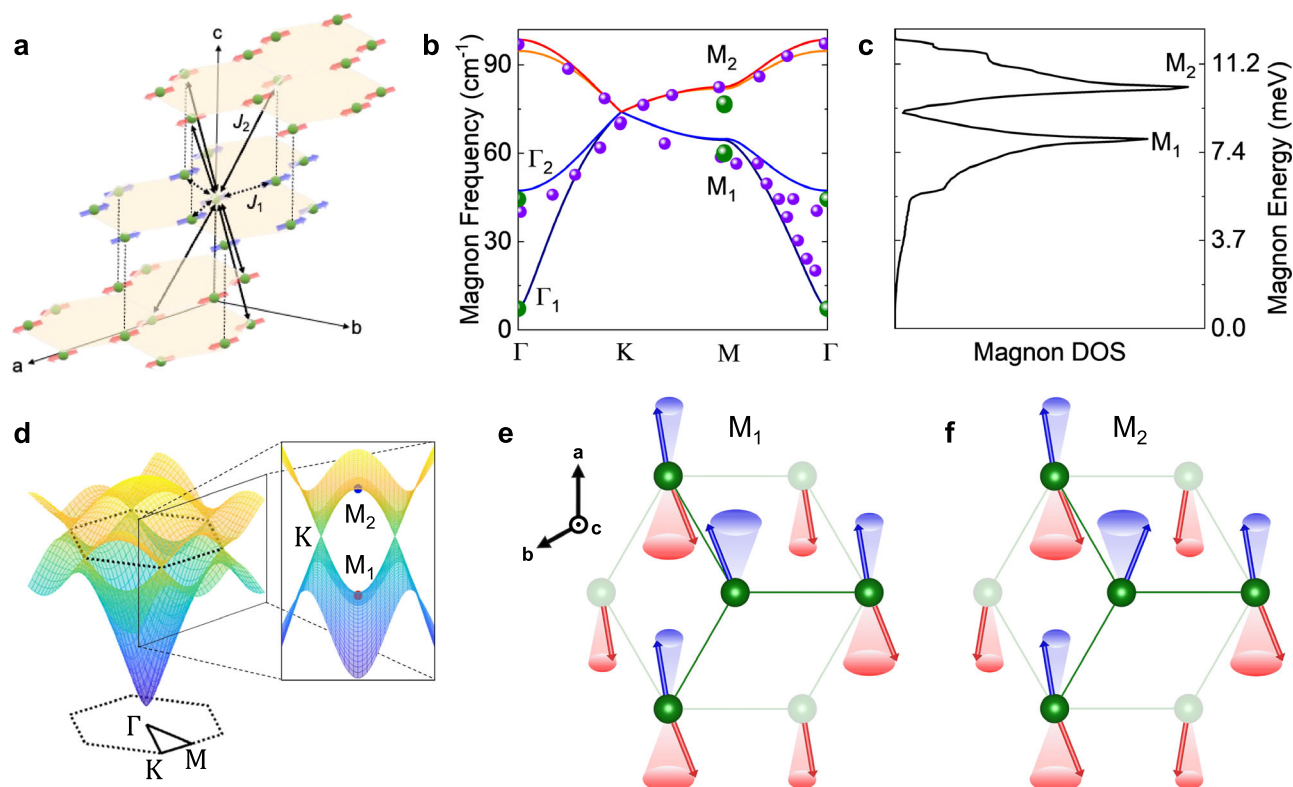
Fig. 1 | Magnons in CoTiO₃. a Spin lattice structure of the buckled honeycomb of Co^{2+} ions in the AFM phase. The spins are ordered ferromagnetically (anti-ferromagnetically) between intralayer (interlayer) spins coupled by the exchange interaction J_1 (J_2). The colored arrows indicate the direction of magnetic moments aligned in the *ab* plane. **b** Calculated magnon dispersion (color solid lines) along the lines of Γ-K-M-Γ in the Brillouin zone. The green and purple dots are experimental data from our Raman measurements and INS from ref. 16, respectively. **c** Magnon density of states (DOS) calculated from the magnon dispersion. **d** Schematics of

magnon dispersion that highlights a linear dispersion at the K point and saddle-points at M_1 (red dot) and M_2 (blue dot) points. The hexagon denotes the zone boundary labeled with high symmetry points. **e, f** Schematic of magnon precession for M_1 and M_2 modes involving two adjacent honeycomb lattices in the *ab* plane. Atoms in the top (bottom) layer are represented by dark (light) green balls and the arrows describe the phases of the precession. Three atoms (with both blue and red cones) in the two layers overlap in this top view along the *c*-axis.

presence of magnon-magnon scattering, overlapping single-magnon bands with two- or three-magnon continua result in magnon damping.[9] Interestingly, in chiral honeycomb ferromagnets, theoretical studies have further identified specific conditions (e.g., external magnetic field and temperature) under which topological phase transitions occur in the presence of magnon interactions[2,3]. Recent experiments based on inelastic neutron scattering (INS)[10,11] and the thermal Hall effect[12,13] have identified several classes of promising materials. However, direct detection of in-gap surface states or images of topologically protected edge states, similar to experiments on electronic topology, is still out of reach[14,15].

Results

Here, we study CoTiO₃ as a model honeycomb AFM insulator with confirmed Dirac magnon bands[16,17]. Using polarization-resolved Raman spectroscopy, we identify multiple magnon peaks via temperature- and magnetic-field-dependent experiments. The saddle points at the high symmetry M points on the Brillouin zone boundary lead to an exceptionally large DOS, thus dominating two-magnon scattering processes. Most intriguingly, these exchange magnons with nan-ometer wavelengths exhibit a significantly sharper linewidth (limited by instrument resolution) than the Γ point magnon at the zone center. This unusual momentum dependence of magnon lifetimes in CTO originates from several combined factors, including the anti-ferromagnetic order, particle number non-conserving interaction, a small joint two-magnon DOS, exchange anisotropy, and single magnon band features. The magnon lifetime decreases in the presence of an

external magnetic field as additional three-magnon decay channels emerge in a non-collinear spin configuration. Our finding establishes new guiding principles for identifying antiferromagnetic insulators for spintronic applications, such as terahertz oscillators and magnon-phonon coupling-based cavities.

The magnetic structure of CoTiO₃ is illustrated in Fig. 1a. The magnetic moments are ordered ferromagnetically within each plane and coupled antiferromagnetically along the *c*-axis. The Co^{2+} ions are arranged in two-dimensional honeycomb lattices that are slightly buckled. They are stacked along the *c*-axis in an ABC sequence with neighboring planes displaced diagonally by a third of the unit cell. The topological magnon dispersions are reproduced in Fig. 1b using a model Hamiltonian $H = \sum_{i\delta} J_1(S_i^x S_{i+\delta}^x + S_i^y S_{i+\delta}^y) + \sum_{i\gamma} J_2(\mathbf{S}_i \cdot \mathbf{S}_{i+\gamma})$ with exchange couplings $J_1 = -4.4$ meV (XY interaction) and $J_2 = 0.57$ meV (isotropic Heisenberg interaction) between pairs of Co^{2+} ions that are labeled by the arrows J_1 and J_2 in Fig. 1a. The coupling parameters are extracted from INS experiments[16,17] (reproduced as purple spheres in Fig. 1b) and suggest a strong easy-plane anisotropy. The Raman measurements (to be presented later) are overlaid as green spheres. The comparison to neutron scattering experiments serves as an important guide in assigning the magnon modes in our Raman spectra.

The magnon density of states (DOS) calculated from the disper-sion is shown in Fig. 1c. At the M points, the DOS is much larger than other high symmetry points in the Brillouin zone, as a consequence of the saddle shape of magnon bands at the M points as illustrated in Fig. 1d. The M_1 (M_2) mode corresponds to an acoustic (optical) mode
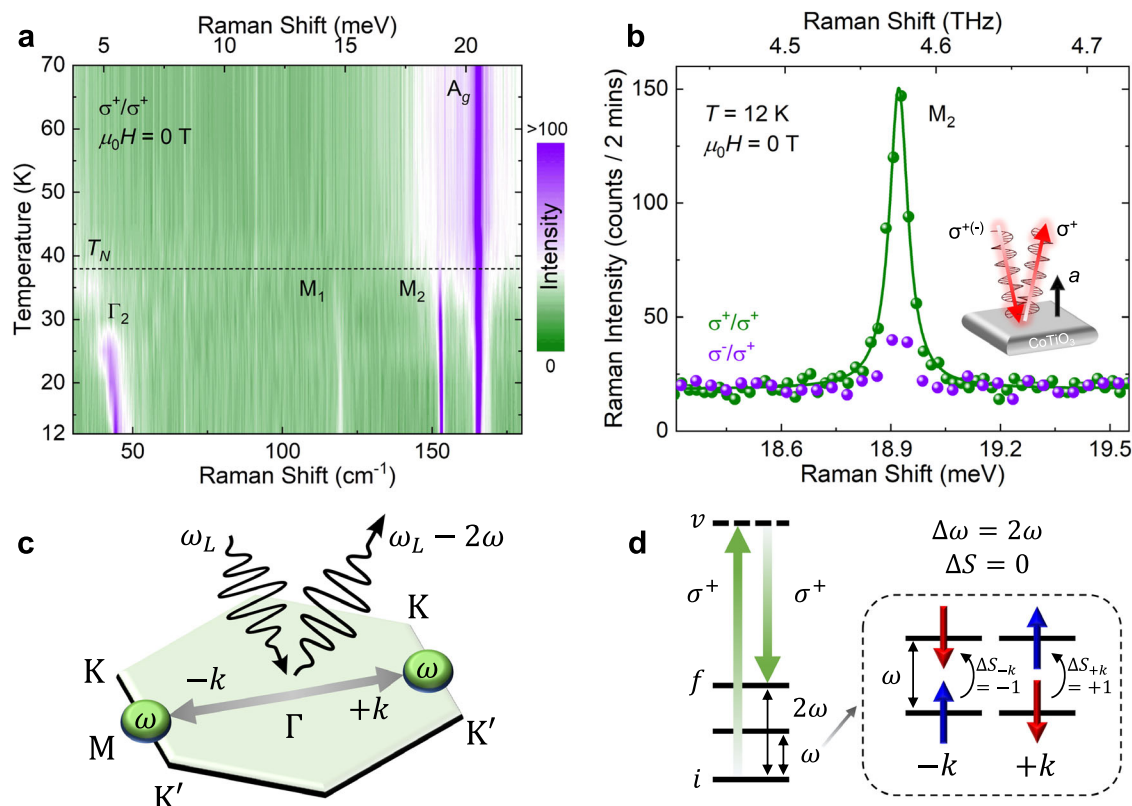
Fig. 2 | Temperature and polarization dependence of Raman spectra identifying magnons and phonons. a temperature-dependent Raman spectra taken at zero field. Multiple magnon modes at high symmetry points (Γ_2, M_1, M_2) are identified in the AFM phase, while a phonon mode (A_g) is observable in both the AFM and PM phases. **b** Polarization-resolved Raman spectra taken at 12 K in the AFM phase. σ^+/σ^+ (green dots) and σ^-/σ^+ (purple dots) represent co- and cross-circularly polarized incident and scattered lights. Green solid line is a Lorentzian fit. Inset

illustrates the back-scattering geometry from a sample with surface normal along the crystalline *a*-axis. **c** Schematic of the Stokes Raman process for two-magnon excitations. **d** Double spin-flip process in the σ^+/σ^+ channel. Two magnons (2ω) with opposite wavevectors $+k$ or $-k$ are optically created via a virtual state and each undergoes a spin-flip. The net angular momentum change ΔS is 0, leading to a 2M signal in the σ^+/σ^+ polarization channel. (*i*: initial state; *f*: final state; *v*: virtual state.).

with in-phase (out-of-phase) precession in a semi-classical picture as illustrated in Fig. 1e,f. The magnetic moments in adjacent layers are oppositely aligned and undergo counter-circular precessions around the *a*-axis. All measurements presented in this report are taken from a sample with its surface normal along the *a*-axis. We make this choice to optimize the signal from the M_2 mode and highlight the unique magnon properties in CTO.

To identify magnons, we compare Stokes Raman spectra taken in two different magnetic phases. In the paramagnetic (PM) phase ($T > T_N \sim 38$ K), a Raman-active phonon peak (A_g) is identified within the spectral range (Fig. 2a). In the AFM phase ($T < T_N$), multiple magnon peaks (Γ_2, M_1, M_2) are observed (more details shown in Supplementary Fig. 1). The energies, as well as the temperature and polarization dependence, of single magnon resonances agree with those measured in INS experiments, validating our comparison between Raman and INS experiments on CTO. We further attribute M_1 and M_2 peaks to two-magnon resonances dominated by the high symmetry M points on the Brillouin zone boundary (M_1, M_2) based on their frequencies in comparison to INS (Fig. 1b), the calculated high DOS (Fig. 1c), and temperature-dependent integrated intensity and peak center (Fig. 3) as further explained below. Because of its strong intensity, we focus on the analysis of M_2 mode (Fig. 2b) in the following. Similarly, we assign the phonon modes based on temperature-dependent and polarization-resolved spectra, which are consistent with prior studies of phonons in CTO[18].

In two-magnon Stokes scattering processes, incident photons (ω_L) create a pair of magnons (ω) so that the frequency of the scattered

photon is shifted by twice the magnon frequency (2ω). The pair of magnons has wavevectors and angular momenta equal in magnitude but opposite in direction as illustrated in Fig. 2c, d. Because the sum of the wave vectors is zero, momentum conservation is satisfied in the light scattering processes where photons carry negligible momentum. In principle, any point in the Brillouin zone can contribute to two-magnon scattering. The contribution from the zone-boundary magnons is enhanced by both a geometrical factor in the scattering cross-section[19] and their unique long lifetimes in CTO. Other zone-boundary magnons (e.g., K points) should also contribute. The higher DOS and its frequency closely matching the INS experiments suggest that the two-magnon resonance primarily originates from M-point magnons. Half of the M_2 magnon energy measured in Raman (green circles) is slightly lower than the single magnon energy measured in INS (purple circles) in Fig. 1b.

The angular momentum conservation requirement is typically manifested by the polarization selection rules. We qualitatively describe the scattering process leading to the M_2 mode in the co-circularly polarized channel. This two-magnon scattering process occurs via an exchange mechanism where a pair of exchange-coupled (J_2) magnetic ions within two spin sub-lattices simultaneously flip their spins upon the virtual electronic excitation as illustrated in Fig. 2d[20]. Consequently, the total angular momentum change (ΔS) is zero, thus, leading to a Raman signal in the co-circularly polarized channel (σ^+/σ^+) as shown in Fig. 2b. While the dominant Raman signal in the co-circularly polarized channel can be qualitatively explained by this simplified picture, we caution that the low symmetry of the magnetic
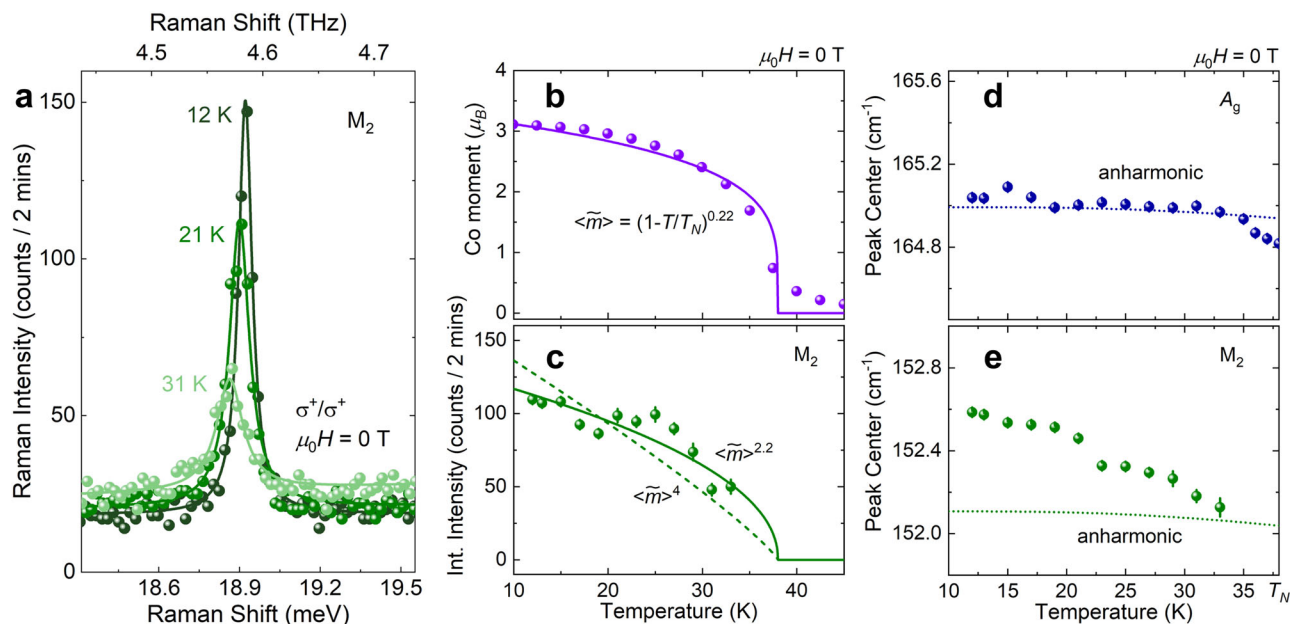
Fig. 3 | Temperature dependence of M_2, Co magnetic moment, and A_g phonon.
a M_2 Raman spectra taken at 12 K, 21 K, and 31 K at zero field in the σ^+/σ^+ channel.
b Co magnetic moment extracted from neutron diffraction data from ref. [17].
Reduced sublattice magnetization $\langle \tilde{m} \rangle$ is fitted to an order parameter-like function
$(1 - T/T_N)^{\beta}$ with $\beta = 0.22$ (purple solid curve). **c** Integrated intensity of M_2. The
green solid curve $\langle \tilde{m} \rangle^{2.2 \pm 0.4}$ is the best fit through the measured Raman integrated
intensity. Data deviates from the function $\langle \tilde{m} \rangle^4$ (green dashed line) predicted and
observed for zone-folded phonons. Peak center of (**d**) A_g phonon and (**e**) M_2 as a
function of temperature. The M_2 frequency shift -0.5 cm^{-1} exceeds that expected
for a zone-folded phonon mode. Dashed lines in (**d**) and (**e**) are predicted frequency
shifts from an anharmonic phonon model. Error bars are obtained from Lorentzian
model fits to Raman peaks.

space group in CTO $P_S\bar{1}$[17] does not constrain the Raman tensor enough
to predict a strict selection rule via group theory[21].

In addition to two-magnon resonances, zone-folded phonons can
also emerge in the AFM phase below the Néel temperature. In order to
rule out this alternative interpretation of the M_2 resonance, we analyze
the temperature-dependent integrated Raman intensity and central
frequency of the M_2 mode. We compare how the sublattice magnetiza-
tion, M_2 and A_g phonon mode evolve below the Néel temperature in
Fig. 3. Raman spectra of M_2 taken at 30 K, 21 K, and 12 K are shown in
Fig. 3a. With decreasing temperature, the M_2 peak exhibits an
increasing integrated intensity and a blue shift in frequency as sum-
marized in Fig. 3c, e. To explain these observations, we extract the Co
sublattice magnetic moment $\langle m \rangle$ temperature dependence from
neutron diffraction data[17] in Fig. 3b. The magnetic moment $\langle m \rangle$
increases with decreasing temperature and saturates toward ~3 μ_B.
The reduced magnetic moment $\langle \tilde{m} \rangle = \langle m \rangle/3\mu_B$ is fitted to an order
parameter-like function $(1 - T/T_N)^{\beta}$, where $T_N = 38$ K and
$\beta = 0.22 \pm 0.02$ (also Supplementary Fig. 9). A two-magnon resonance
is expected to scale with $\langle \tilde{m} \rangle^2$ while a zone-folded phonon mode scales
with $\langle \tilde{m} \rangle^4$ as shown in CoPS$_3$ and FePS$_3$ previously[22–24]. The fitting for
the temperature-dependent M_2 Raman intensity yields $\langle \tilde{m} \rangle^{2.2 \pm 0.4}$. In
Fig. 3c and e, we plot calculated intensity and frequency shift (dashed
lines) if M_2 were a zone-folded phonon. The deviations between the
measurements and phonon-based models support our assignment of
M_2 to a two-magnon resonance. We further identify the 228 cm^{-1} peak
as a zone-folded phonon mode in CTO and confirm that its
temperature-dependent integrated intensity follows the $\langle \tilde{m} \rangle^4$ predic-
tion (Supplementary Fig. 3).

Next, we analyzed the temperature-dependent peak center shift
for the nearby A_g phonon (Fig. 3d) and M_2 modes (Fig. 3e). Both
phonon population and frequency are expected to change with tem-
perature. However, for a high-frequency optical phonon, the anhar-
monic model[25] (see dashed line in Fig. 3d) predicts a near constant
frequency (<0.1 cm^{-1}) due to the small variation in the population of

thermal phonons over this low-temperature range. In contrast, the
frequency of the M_2 mode shifts by ~0.5 cm^{-1}, exceeding that expected
of a phonon mode, again validating the assignment of M_2 as a two-
magnon resonance. We note that the M_1 peak also follows the same
trends (See Supplementary Fig. 2), confirming that the properties of
both M_1 and M_2 follow those predicted for two-magnon resonances.

While two-magnon resonances are commonly observed in Raman
spectra of AFM insulators[26–28], the narrow linewidth of the M_2 peak
observed in CTO is remarkable. The magnon spectra shown in Fig. 4a
are taken at zero field (green) and with a 5 T field (blue) applied along
the a-axis. The M_2 linewidth at zero field is limited by the instrument
resolution indicated by the gray vertical stripe. The linewidth broadens
when the external magnetic field parallel to the a-axis, i.e., $\mu_0 H \| a$,
increases as shown in Fig. 4b. This field-dependent line width can be
partially attributed to additional decay channels arising from three-
magnon interactions enabled in a non-collinear spin configuration (see
Methods). A two-magnon resonance is spectrally broadened when
either one of the two magnons with opposite momentum decays.
Thus, half of the two-magnon resonance linewidth provides a lower
bound on the single-magnon lifetime <25 ps.

To understand the origin of the long lifetime of zone-boundary
magnons in CTO, we first examine their possible decay channels. In
insulators, magnons primarily decay through two mechanisms:
magnon-phonon and magnon-magnon interactions. Magnon and
phonon coupling is strongest when their dispersions cross[29–32]. In CTO,
however, both the acoustic and optical phonon modes have higher
energies than magnons at the zone boundary, thus reducing the
magnon-phonon coupling[33]. Specifically, the M_2 and A_g peaks are
clearly separated at 12 K (see Fig. 2a). Both spectral line shapes are
symmetric (Lorentzian), indicating the absence of quantum inter-
ference between magnon and phonon modes. We also perform
temperature-dependent measurements for the M_2 decay rate and
identify a $T^{1.8}$ dependence, which supports magnon-magnon
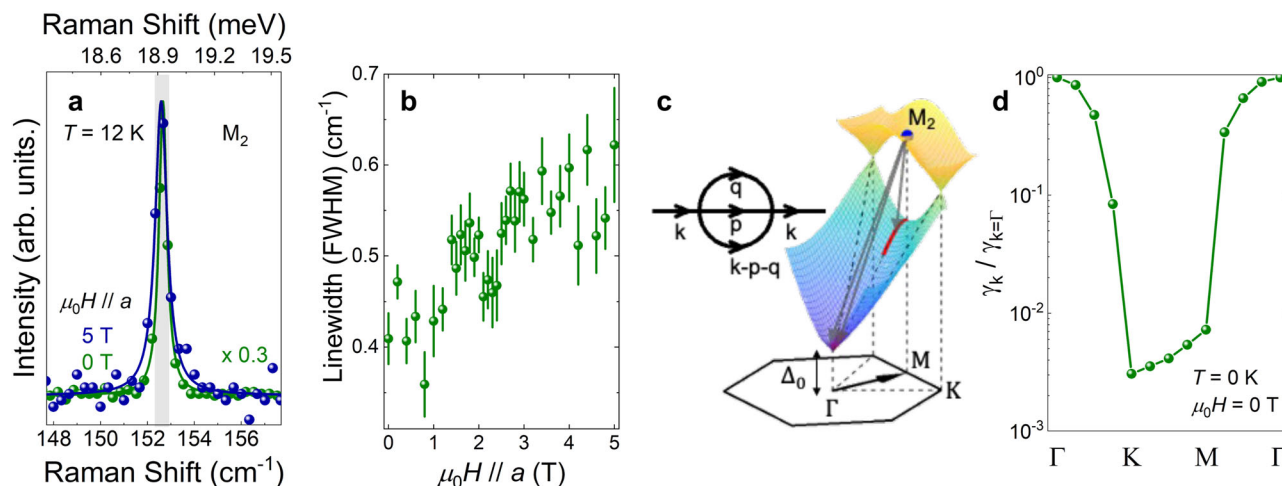scattering[34–36] as the dominant magnon decay channel rather than

Fig. 4 | Measured and calculated M₂ damping. a M₂ Raman resonance measured at zero field (green) and 5 T (blue). Solid lines are Lorentzian fits and the linewidth for the $\mu_0 H = 0$ spectrum is limited by the instrument resolution, indicated by gray vertical strip. **b** Measured magnetic field dependence of M₂ linewidth extracted from Lorentzian fits. Error bars are obtained from Lorentzian model fits to Raman peaks. **c** M₂ magnon decays to lower energy magnons (gray arrows) via a four-magnon process illustrated by the Feynman diagram. The lowest magnon energy is gapped (Δ_0) at the Γ point. As a result, four-magnon decay process is restricted (the red region) considering both the energy and momentum conservation. **d** Calculated magnon decay rate (normalized by Γ point magnon) along a high-symmetry path at zero field and 0 K, showing ~140 fold reduction for the zone-boundary magnons.

magnon-phonon scattering that should follow T^5 [37] (see Supplementary Fig. 12). Therefore, we focus on modeling magnon-magnon interactions below. The two-magnon continuum often overlaps with single-magnon bands at the zone boundary, leading to a rapid magnon decay. Thus, zone-boundary magnon modes typically exhibit a shorter lifetime than those at the zone center in common AFMs such as MnF₂ and NiO [9,38]. Thus, the significantly narrower linewidth of zone boundary M₂ magnons than zone-center Γ point magnons in CTO is a surprising observation.

To calculate the momentum-dependent magnon lifetime resulting from magnon-magnon interactions, we follow the procedure outlined below. This analysis not only provides insights into why other common AFM materials typically exhibit short-lived zone-boundary magnons but also establishes a framework for identifying long-lived zone-boundary magnons in other materials. We begin with the general spin model $H = \sum_{i\delta} J_1 (S_i^x S_{i+\delta}^x + S_i^y S_{i+\delta}^y + \alpha S_i^z S_{i+\delta}^z) + \sum_{i\gamma} J_2 (\mathbf{S}_i \cdot \mathbf{S}_{i+\gamma})$ with exchange couplings $J_1 = -4.4$ meV and $J_2 = 0.57$ meV. While the best and most precise Hamiltonian for CoTiO₃ is still under debate [17,39–41], these models predict the same magnon dispersion measured by INS experiments. Thus, the choice among these Hamiltonians does not alter the calculated magnon lifetimes, considering the assumptions adopted as described in "Methods". For $\alpha = 0$, we recover the model for CTO, while for $\alpha = 1$, we obtain an isotropic in-plane exchange interaction suitable for many van der Waals magnets such as CrI₃. Subsequently, we perform a Dyson-Maleev transformation to obtain the interacting magnon Hamiltonian, expressed as $H = H_{(0)} + H_{(2)} + H_{(3)} + H_{(4)} + \cdots$, where $H_{(0)}$ defines the ground state, $H_{(2)}$ is the non-interacting magnon Hamiltonian usually used to predict band topology, and $H_{(3)}$ ($H_{(4)}$) corresponds to the three (four)-magnon interaction (expressions are provided in the Methods section). These interaction terms are directly proportional to the magnetic exchange constants and give rise to finite magnon lifetimes. In the collinear AFM configuration at zero field, 3-magnon scattering is prohibited by spin-rotational symmetry around the Nèel vector direction [42].

Assuming zero temperature and zero external magnetic field, the dominant decay channel for M₂ magnons corresponds to four-magnon decay processes in which one higher energy magnon spontaneously decays into three lower energy magnons as represented by the Feynman diagram in Fig. 4c. Multi-magnon decays arise from interactions between magnons with the bosonic character that the particle number is not conserved. Strikingly, our numerical evaluation of the momentum-dependent magnon lifetime predicts that the zone boundary magnon decay rate is lower by a factor of ~140 than that for zone-center magnons in CTO as shown in Fig. 4d. We present the details of the momentum-dependent magnon lifetime calculations in Methods. We assume a constant parameter for matrix elements (see Methods) that may lead to a factor of 2 uncertainty in the predicted lifetimes. These calculations are meant to capture the key elements responsible for the momentum-dependent magnon lifetimes, rather than a quantitative prediction of magnon lifetimes in CTO. The long-lived zone-boundary magnon in CTO can be partially attributed to a reduced joint two-magnon DOS (see Methods), consistent with a prior theoretical study on honeycomb-lattice XXZ AFMs [43]. The observed magnetic-field-dependent magnon linewidths (Fig. 4b) are readily explained by the additional three magnon scattering processes enabled in the non-collinear spin configuration in the presence of an external field. The three-magnon decay phase space is proportional to the two-magnon DOS, $D(\mathbf{q}, E) = \frac{1}{N} \sum_{l,m} \sum_{\mathbf{p}} \delta(E - \varepsilon_{\mathbf{p},l} - \varepsilon_{\mathbf{q}-\mathbf{p},m})$. Our calculation confirms a larger number of decay channels at a finite magnetic field as shown in Supplementary Fig. 6. Although our experiments focused on M point magnons due to their higher DOS, Dirac magnons at K points may also exhibit longer lifetimes in CTO as shown in our calculated momentum-dependent lifetimes in Fig. 4d. Future experimental studies based on the neutron echo technique may confirm this prediction.

From a theoretical perspective, a honeycomb spin lattice with an interaction-induced magnon gap near the Dirac cone is expected to lead to topologically protected states. Among the materials proposed for topological magnons, three-magnon scattering is forbidden in AFMs generally and in selected FMs with spin-rotation symmetry [42]. Additionally, those with well-separated phonon and magnon energies likely exhibit reduced phonon-magnon interaction-induced decay. CTO satisfies these simple principles. Our calculation, taking into account the specific magnon dispersion of CTO, also highlights that a shallow magnon dispersion combined with a sizable magnon gap (Δ_0) at the Γ point restricts the kinetic mechanism for magnon-magnon interaction-induced decay. Furthermore, exchange anisotropy ($\alpha = 0$ in the generalized model) is found to be an unexpected yet critical

element for long magnon lifetimes. Empirically, a few families of honeycomb Van der Waals magnets including $CrGe(Si)Te_3$, CrX_3 (X = Cl, Br, I), and MPS_3 (M = Mn, Fe, Ni, Co)[10,44-48] have been proposed or confirmed to host topological magnons but they all exhibit isotropic exchange interaction. We provide a survey of these alternative topological magnon materials in Supplementary Table 1. By calculating momentum-dependent magnon lifetimes in both CTO and CrI_3 (Methods and Supplementary Figs. 7 and 14), our studies suggest that a strong exchange anisotropy (XXZ-like magnon Hamiltonian) may be another critical element for long-lived zone-boundary magnons that has been largely ignored in previous studies.

In summary, we discovered unusual magnon properties at the high symmetry points along the Brillouin zone boundary in CTO that hosts Dirac magnon bands. Because the saddle points in the magnon dispersion exhibit a large DOS, efficient two-magnon scattering processes allow us to observe large momentum magnons with nanometer wavelength. In contrast to other common AFMs, the zone-boundary magnons exhibit significantly longer lifetimes than those at the zone center. Our calculations explain the observed momentum- and field-dependent magnon linewidths. While we did not detect the elusive surface or edge states protected by topology, our study articulates several elements necessary to support long-lived magnons, including AFM order, the small joint two-magnon DOS, exchange anisotropy, and single magnon bands. A long magnon lifetime is a necessary condition for both the detection of and harvesting the benefits of topologically protected states. By going beyond the single-particle topology and taking into account higher-order terms in the spin Hamiltonian, future computational searches can help to identify promising candidate materials for room-temperature topological magnons[49].

Methods

Sample growth and characterization
High-quality $CoTiO_3$ single crystals were prepared using the floating zone method. Starting ceramic rods of $CoTiO_3$ were prepared by solid state reaction of thoroughly mixed stoichiometric of CoO (99.99%, Alfa Aesar) and TiO_2 (99.99%, Alfa Aesar) at 1000 °C in air. The crystal growth in the image furnace was carried out with a constant air flow and 8 mm/h of growth speed. $CoTiO_3$ single crystal is black in color and the surface is shiny. The phase purity of $CoTiO_3$ was confirmed by powder X-ray diffraction with the powder sample made by crushing single crystals. The sample orientation was determined by Laue back reflection method.

Raman spectroscopy
Raman measurements of CTO samples were performed using a 632.81 nm excitation laser in the back-scattering geometry. The laser power of 0.1 mW was used to minimize the heating effect. The scattered light was collected for 2 min integration time, dispersed by an 1800-mm^{-1} groove-density grating, and detected by a thermoelectric-cooled CCD. The Raman shift difference between adjacent pixels of CCD was 0.34 cm^{-1}. The samples were mounted in a cryostat capable of reaching temperature down to 10 K. A superconducting magnet was used to apply out-of-plane magnetic fields up to 5 T.

Magnon dispersion calculations
The XXZ Hamiltonian with anisotropy exchange coupling is transformed by applying the Holstein-Primakoff transformation and reduced to $H = \sum_{\mathbf{k}} \mathbf{\Phi}_{\mathbf{k}}^{\dagger} \mathcal{D}(\mathbf{k}) \mathbf{\Phi}_{\mathbf{k}}$, where $\mathbf{\Phi}_{\mathbf{k}}^{\dagger} = (a_k^{\dagger}, b_k^{\dagger}, c_k^{\dagger}, d_k^{\dagger}, a_{-k}, b_{-k}, c_{-k}, d_{-k})$ and each of the operators a, b, c, and d annihilate magnons with momentum k in the corresponding sublattice. The matrix $\mathcal{D}(\mathbf{k})$ is given by

$$\mathcal{D}(\mathbf{k}) = \begin{pmatrix} \mathbf{A}(\mathbf{k}) & \mathbf{B}(\mathbf{k}) \\ \mathbf{B}^{\dagger}(\mathbf{k}) & \mathbf{A}^{*}(-\mathbf{k}) \end{pmatrix} \tag{1}$$

where, the matrices $\mathbf{A}(\mathbf{k})$ and $\mathbf{B}(\mathbf{k})$ are given by

$$\mathbf{A}(\mathbf{k}) = \begin{pmatrix} -z_1 S J_1 + z_\perp S J_2 & S J_1 (1 + \frac{\alpha}{2}) f_{\mathbf{k}} & 0 & 0 \\ S J_1 (1 + \frac{\alpha}{2}) f_{\mathbf{k}}^* & -z_1 S J_1 + z_\perp S J_2 & 0 & 0 \\ 0 & 0 & -z_1 S J_1 + z_\perp S J_2 & S J_1 (1 + \frac{\alpha}{2}) f_{\mathbf{k}} \\ 0 & 0 & S J_1 (1 + \frac{\alpha}{2}) f_{\mathbf{k}}^* & -z_1 S J_1 + z_\perp S J_2 \end{pmatrix}, \tag{2}$$

$$\mathbf{B}(\mathbf{k}) = \begin{pmatrix} 0 & S J_1 \frac{\alpha}{2} f_{\mathbf{k}} & S J_2 f_{ac\perp, -\mathbf{k}} & S J_2 f_{ad\perp, -\mathbf{k}} \\ S J_1 \frac{\alpha}{2} f_{\mathbf{k}}^* & 0 & S J_2 f_{bc\perp, -\mathbf{k}} & S J_2 f_{bd\perp, -\mathbf{k}} \\ S J_2 f_{ac\perp, -\mathbf{k}}^* & S J_2 f_{bc\perp, -\mathbf{k}}^* & 0 & S J_1 \frac{\alpha}{2} f_{\mathbf{k}} \\ S J_2 f_{ad\perp, -\mathbf{k}}^* & S J_2 f_{bd\perp, -\mathbf{k}}^* & S J_1 \frac{\alpha}{2} f_{\mathbf{k}}^* & 0 \end{pmatrix}, \tag{3}$$

$f_{\mathbf{k}} = \sum_{\boldsymbol{\delta}} e^{i\mathbf{k}\cdot\boldsymbol{\delta}}$, and $z_1 = 3$ are the number of intra-plane nearest-neighbors, $f_{ac\perp,\mathbf{k}} = f_{bd\perp,\mathbf{k}} = \sum_{\boldsymbol{\gamma}} e^{i\mathbf{k}\cdot\boldsymbol{\gamma}}$, $f_{ad\perp,\mathbf{k}} = \sum_{\boldsymbol{\gamma}} e^{i\mathbf{k}\cdot\boldsymbol{\gamma}_-}$, $f_{bc\perp,\mathbf{k}} = \sum_{\boldsymbol{\gamma}} e^{i\mathbf{k}\cdot\boldsymbol{\gamma}_+}$, and $z_\perp$ is the number of interlayer A−C next-nearest-neighbors. $\boldsymbol{\gamma}_{\mp}$ correspond to the interlayer nearest-neighbor vectors for A-D sublattices (− sign) and B–C (+ sign) sublattices. The magnon energies are obtained by diagonalizing $\hat{g}\mathcal{D}(\mathbf{k})$ numerically, where $\hat{g} = [1, 1, 1, 1, -1, -1, -1, -1]$[50]. The presence of a spin-wave gap at the Γ point lies beyond the XXZ model, and its origin is still under debate[17]. Here, we add a phenomenological term of the form $H_\eta = \frac{\eta}{2} \sum_{i,\boldsymbol{\delta}} \left(\tilde{S}_i^y \tilde{S}_{i+\boldsymbol{\delta}}^y - \tilde{S}_i^x \tilde{S}_{i+\boldsymbol{\delta}}^x \right)$, which leads to a gap at the Γ point. We used $\eta = 0.05$ meV, which reproduces the low magnon energy of ~1 meV observed in neutron scattering measurements[16,17].

Magnon lifetime calculations
In this section, we discuss general aspects of the magnon lifetime, arising from magnon–magnon interactions. To obtain the interaction potential, we perform a Dyson-Maleev transformation[51] on the spin Hamiltonian. The interacting magnon Hamiltonian can be written as $H = H_{(0)} + H_{(2)} + H_{(3)} + H_{(4)} + \cdots$. Here, $H_{(0)}$ corresponds to the classical energy and defines the ground state[42]. $H_{(2)}$ is the noninteracting magnon Hamiltonian leading to the magnon bands as discussed in the previous sections. $H_{(3)}$ and $H_{(4)}$ correspond to the three- and four-magnon interaction terms.

We start with the zero-field case. We find $H_{(3)} = 0$, and

$$\begin{aligned} H_{(4)} = &\left[\sum_{1234} \left[J_1 \delta(1-2+3-4) f_{4-3} a_1^{\dagger} a_2 b_3^{\dagger} b_4 + \frac{J_1}{2} \delta(1+2-3-4) f_{-2+3+4} \left(-1 + \frac{\alpha}{2} \right) a_1^{\dagger} b_2^{\dagger} b_3 b_4 \right. \right. \\ &+ \frac{J_1}{2} \delta(1-2-3+4) f_{-4} \left(-1 + \frac{\alpha}{2} \right) a_1^{\dagger} a_2 a_3 b_4^{\dagger} + \frac{J_1 \alpha}{4} \delta(1-2-3-4) f_4 a_1^{\dagger} a_2 a_3 b_4 \\ &\left. + \frac{J_1 \alpha}{4} \delta(-1+2-3-4) f_{-2+3+4} a_1 b_2^{\dagger} b_3 b_4 \right] + [(a,b) \rightarrow (c,d)] \right] \\ &- \left[\frac{J_2}{2} \sum_{1234} \left[\delta(1-2-3-4) g_4 a_1^{\dagger} a_2 a_3 c_4 + 2\delta(1-2+3-4) g_{-3+4} a_1^{\dagger} a_2 c_3^{\dagger} c_4 \right. \right. \\ &\left. + \delta(1+2+3-4) g_{-2-3+4} a_1^{\dagger} c_2^{\dagger} c_3^{\dagger} c_4 \right] \\ &\left. + [(a,c,\gamma) \rightarrow (b,d,\gamma) + (a,c,\gamma) \rightarrow (a,d,\gamma_-) + (a,c,\gamma) \rightarrow (b,c,\gamma_+)] \right] \end{aligned}$$

where $f_{\mathbf{k}} = \sum_{\boldsymbol{\delta}} e^{i\mathbf{k}\cdot\boldsymbol{\delta}}$, $g_{\mathbf{k}} = \sum_{\boldsymbol{\gamma}} e^{i\mathbf{k}\cdot\boldsymbol{\gamma}}$, and δ is the intralayer nearest-neighbor distance and γ the interlayer nearest-neighbor distance between sublattices a, c; $\boldsymbol{\gamma}_-$ is between a, d; and $\boldsymbol{\gamma}_+$ is between b, c. The numbers 1, 2, 3, 4 label the momenta $\mathbf{k}_1, \mathbf{k}_2, \mathbf{k}_3, \mathbf{k}_4$, respectively. The expression for $H_{(4)}$ contains terms that correspond to magnon-conserving two-magnons-in/two-magnons-out processes (such as $a_1^{\dagger} a_2 b_3^{\dagger} b_4$), and decay and recombination of one magnon into three magnons (such as $a_1^{\dagger} a_2 a_3 b_4$). The later terms that do not conserve the number of magnons are allowed in antiferromagnets because the ground state is a superposition of states with different total spin[42,51,52]. Diagrammatic representations of these terms are shown in Supplementary Fig. 4a[42] and b[3].

The decay and recombination of one magnon into three magnons (Supplementary Fig. 4a) leads to a magnon lifetime of the form (at zero

temperature)[42]

$$\Gamma_{\mathbf{k}}^{(4a)} = \frac{\pi}{6N^2} \sum_{\mathbf{q},\mathbf{p}} |V_{4a}(\mathbf{q},\mathbf{p};\mathbf{k})|^2 \delta\big(\varepsilon_{\mathbf{k}} - \varepsilon_{\mathbf{q}} - \varepsilon_{\mathbf{p}} - \varepsilon_{\mathbf{k}-\mathbf{q}-\mathbf{p}}\big), \quad (4)$$

where ε are the magnon energies, and $V_{4a}(\mathbf{q},\mathbf{p};\mathbf{k})$ is the momentum-dependent matrix element.

The two-magnons-in/two-magnons-out scattering processes (Supplementary Fig. 4b) lead to a contribution to the lifetime[3]

$$\Gamma_{\mathbf{k}}^{(4b)} = \frac{\pi}{6N^2} \sum_{\mathbf{q},\mathbf{p}} |V_{4b}(\mathbf{q},\mathbf{p};\mathbf{k})|^2 F(\mathbf{q},\mathbf{p};\mathbf{k}) \delta\big(\varepsilon_{\mathbf{k}} + \varepsilon_{\mathbf{q}} - \varepsilon_{\mathbf{p}} - \varepsilon_{\mathbf{k}+\mathbf{q}-\mathbf{p}}\big), \quad (5)$$

where $F(\mathbf{q},\mathbf{p};\mathbf{k}) = [1 + f(\varepsilon_{\mathbf{p}})][1 + f(\varepsilon_{\mathbf{k}+\mathbf{q}-\mathbf{p}})]f(\varepsilon_{\mathbf{q}}) - f(\varepsilon_{\mathbf{p}})f(\varepsilon_{\mathbf{k}+\mathbf{q}-\mathbf{p}})$ $[1 + f(\varepsilon_{\mathbf{q}})]$, $f(\varepsilon_{\mathbf{q}}) = 1/[\exp(\varepsilon_{\mathbf{q}}/T) - 1]$ accounts for its temperature dependence.

Assuming that the matrix elements are a smooth function of momentum, we approximate them with their average over momentum, $V_{4a(b)}(\mathbf{q},\mathbf{p};\mathbf{k}) \to \langle V_{4a(b)} \rangle$ in Eqs. (4) and (5). We label the magnons bands $m_1(\mathbf{k})$, $m_2(\mathbf{k})$, $m_3(\mathbf{k})$, $m_4(\mathbf{k})$, where $m_1(\mathbf{k})$ corresponds to the lowest and $m_4(\mathbf{k})$ to the highest energy band.

We now analyze the magnon inverse lifetime arising from spontaneous decay (Eq. (4)), considering different possible decay channels. We numerically integrate Eq. (4) with momentum-averaged matrix elements using a Monte Carlo approach with 1200^2 k-points randomly chosen in the BZ. The energy-conserving delta function is broadened with a factor of 10^{-2} meV. We compute the inverse magnon lifetime arising from decaying processes $m_4(\mathbf{k}) \to m_i(\mathbf{q}) + m_j(\mathbf{p}) + m_l(\mathbf{k} - \mathbf{p} - \mathbf{q})$ for $i, j, l = 1, 2, 3, 4$ and find that the dominant channels involve magnons in the two lowest energy magnon bands. This is a consequence of a reduced two-magnon DOS, as we discuss later in the text. The decay channel $m_4(\mathbf{k}) \to m_1(\mathbf{q}) + m_1(\mathbf{p}) + m_1(\mathbf{k} - \mathbf{p} - \mathbf{q})$ is shown in Fig. 4d in the main text. This decay channel is the dominant one for temperatures much lower than the scale set by the magnon gap, $T \approx 10.9$ K.

Next, we consider the magnon spectral broadening due to thermal decays (e.g., two-magnons-in and two-magnons-out processes (Eq. (5)), with momentum-averaged matrix elements. We use a Monte Carlo approach with 1600^2 k-points randomly chosen in the BZ. Since at 12 K only the magnon band m_1 is thermally occupied near the Γ point, the dominant decay channel for a $m_4(\mathbf{k})$ magnon is of the form $m_4(\mathbf{k}) + m_1(\mathbf{q} \approx \Gamma) \to m_i(\mathbf{p}) + m_j(\mathbf{k} - \mathbf{p} - \mathbf{q})$, with $i, j = 1, 2$. In Supplementary Fig. 13, we plot the inverse lifetime arising from the decay channel $m_4(\mathbf{k}) + m_1(\mathbf{q} \approx \Gamma) \to m_1(\mathbf{p}) + m_1(\mathbf{k} - \mathbf{p} - \mathbf{q})$ for a set of temperatures up to 20 K. We assume $\langle V_{4b} \rangle = \alpha \langle V_{4a} \rangle$, with $\alpha = 1$. However, a different α would scale the magnon spectral broadening due to thermal decay processes. The experimental measurements indicate $\alpha < 1$.

In the magnon lifetime calculations, from equations (4) and (5), we additionally assumed that the matrix elements are independent of the magnon wavefunctions and were approximated with a constant parameter. This simplification (in addition to the general assumptions outlined above) could lead to a factor of 2 or more differences in the predicted linewidth. The theory is not intended for a quantitative agreement but to identify the leading qualitative factors. We expect more sophisticated calculations will follow our experimental work.

For finite magnetic fields $H_z \| a$, we find the three-magnon interactions

$$H_{(3)} = \sum_{123} \Big[\frac{g\mu_B H_z}{2\sqrt{2S}} (\cos\theta - i\sin\theta)\delta(1-2-3)(a_1^\dagger a_2 a_3 + b_1^\dagger b_2 b_3) \Big] + [(a,b,\theta) \to (c,d,-\theta)],$$

where θ is the canting angle. The presence of additional decay channels from three-magnon interactions indicates that shorter lifetimes are naturally expected in non-colinear spin configuration, compared

with the colinear spin. The four-magnon potential takes the form

$$
\begin{aligned}
H_{(4)} = J_1 \Bigg(&\sum_{1234} \Big[\delta(1-2+3-4)f_{4-3}a_1^\dagger a_2 b_3^\dagger b_4 - \frac{1}{2}\delta(1-2-3+4)f_{-4}a_1^\dagger a_2 a_3 b_4^\dagger \\
&- \frac{1}{2}\delta(1+2-3-4)f_{-2+3-4}a_1^\dagger b_2^\dagger b_3 b_4 \\
&- \frac{\alpha}{4}\delta(1-2-3+4)f_{-4}a_1^\dagger a_2 a_3 b_4^\dagger - \frac{\alpha}{4}\delta(1+2-3-4)f_{-2+3-4}a_1^\dagger b_2^\dagger b_3 b_4 \\
&- \frac{\alpha}{4}\big(\cos^2\theta - \sin^2\theta\big)(\delta(1-2-3-4)f_4 a_1^\dagger a_2 a_3 b_4 + \delta(-1+2-3-4)f_{-2+3-4}a_1 b_2^\dagger b_3 b_4) \\
&+ \frac{i\alpha}{2}\cos\theta\sin\theta\big(\delta(1-2-3-4)f_4 a_1^\dagger a_2 a_3 b_4 + \delta(-1+2-3-4)f_{-2+3-4}a_1 b_2^\dagger b_3 b_4\big] \\
&+ [(a,b,\theta) \to (c,d,-\theta)]\Big) \\
&- \Bigg(\frac{J_2}{2}\sum_{1234}\Big[\delta(1-2-3+4)g_{-4}a_1^\dagger a_2 a_3 c_4^\dagger - 2\delta(1-2+3-4)g_{-3+4}a_1^\dagger a_2 c_3^\dagger c_4 \\
&+ \delta(1+2-3-4)g_{-2+3+4}a_1^\dagger c_2^\dagger c_3 c_4 \Big] \\
&+ [(a,c,\gamma) \to (b,d,\gamma) + (a,c,\gamma) \to (a,d,\gamma_-) + (a,c,\gamma) \to (b,c,\gamma_+)]\Bigg).
\end{aligned}
$$

The number of decay channels proportional to J_2 is the same as at zero field, but we obtained four more channels proportional to J_1 at the four-magnon interaction level. The structure of the expressions for the magnon lifetime is the same as at zero field. We note that additional terms could be present in the Hamiltonian due to the non-colinear magnetic moment orientation for finite applied magnetic field.

We also analyze the non-interacting two-magnon DOS, defined as[53]

$$D(\mathbf{q}, E) = \frac{1}{N} \sum_{l,m} \sum_{\mathbf{p}} \delta(E - \varepsilon_{\mathbf{p},l} - \varepsilon_{\mathbf{q}-\mathbf{p},m}), \quad (6)$$

where N is a normalization factor. $D(\mathbf{q}, E)$ quantifies the phase space for the decay of two magnons. This is a relevant quantity because it appears explicitly in the magnon lifetime when we approximate the matrix element with its average over momentum $\langle V_4 \rangle$. For example, we can express the contribution from Supplementary Fig. 4a as $\Gamma_{\mathbf{k}}^{(4a)} \approx \frac{\pi}{6N}\sum_{\mathbf{q};ij}|\langle V_4 \rangle|^2 \int dE \delta(E - \varepsilon_{\mathbf{k},i} + \varepsilon_{\mathbf{q},j})D(\mathbf{k}-\mathbf{q},E)$. In Supplementary Fig. 5, we plot $D(\mathbf{q}, E)$ along a high-symmetry path in the BZ as a function of energy. At the boundary of the BZ, the two-magnon DOS is small compared with the Γ point.

We plot the non-interacting two-magnon DOS $D(\mathbf{q}, E)$ for the magnon energies of M_1 and M_2 and compare between 0 T and 4.5 T (Supplementary Fig. 6). The number of magnon decay channels at zone boundary is highly suppressed for M_1 magnons, indicating longer magnon lifetime. M_2 magnons exhibit relatively smaller decay rates compared to Γ point. Both M_1 and M_2 magnons show the increasing number of decay channel at the finite field.

To justify our model and provide a meaningful comparison to CTO, we calculated the magnon lifetime of CrI_3 at zero magnetic field, an extensively studied material with confirmed Dirac magnon dispersion (see Supplementary Fig. 14). As opposed to CTO, bulk CrI_3 is ferromagnetic with isotropic exchange interactions and a gapped Dirac dispersion at the K-point[54]. We found that, despite the underlying hexagonal layered structure of the lattice, the M-point magnons are not significantly longer-lived than the Γ-point magnons, different from CTO.

Data availability

References

1. McClarty, P. A. Topological magnons: a review. *Annu. Rev. Condens. Matter Phys.* **13,** 171–190 (2021).
2. Mook, A., Plekhanov, K., Klinovaja, J. & Loss, D. Interaction-stabilized topological magnon insulator in ferromagnets. *Phys. Rev. X* **11**, 021061 (2021).

3. Pershoguba, S. S. et al. Dirac magnons in honeycomb ferromagnets. *Phys. Rev. X* **8**, 011010 (2018).
4. Zhang, L., Ren, J., Wang, J.-S. & Li, B. Topological magnon insulator in insulating ferromagnet. *Phys. Rev. B* **87**, 144101 (2013).
5. Wang, X. S., Su, Y. & Wang, X. R. Topologically protected unidirectional edge spin waves and beam splitter. *Phys. Rev. B* **95**, 014435 (2017).
6. Chernyshev, A. & Maksimov, P. Damped topological magnons in the kagome-lattice ferromagnets. *Phys. Rev. lett.* **117**, 187203 (2016).
7. Koyama, S. & Nasu, J. Flavor-wave theory with quasiparticle damping at finite temperatures: application to chiral edge modes in the Kitaev model. *Phys. Rev. B.* **108**, 235162 (2023).
8. Habel, J., Mook, A., Willsher, J. & Knolle, J. Breakdown of chiral edge modes in topological magnon insulators. *Phys. Rev. B* **109**, 024441 (2024).
9. Bayrakci, S., Keller, T., Habicht, K. & Keimer, B. Spin-wave lifetimes throughout the Brillouin zone. *Science* **312**, 1926–1929 (2006).
10. Chen, L. et al. Topological spin excitations in honeycomb ferromagnet CrI$_3$. *Phys. Rev. X* **8**, 041028 (2018).
11. Bao, S. et al. Discovery of coexisting Dirac and triply degenerate magnons in a three-dimensional antiferromagnet. *Nat. Commun.* **9**, 1–7 (2018).
12. Onose, Y. et al. Observation of the magnon Hall effect. *Science* **329**, 297–299 (2010).
13. Zhang, H. et al. Anomalous thermal Hall effect in an insulating van der waals magnet. *Phys. Rev. Lett.* **127**, 247202 (2021).
14. Chen, Y. et al. Experimental realization of a three-dimensional topological insulator, Bi2Te3. *Science* **325**, 178–181 (2009).
15. Drozdov, I. K. et al. One-dimensional topological edge states of bismuth bilayers. *Nat. Phys.* **10**, 664–669 (2014).
16. Yuan, B. et al. Dirac magnons in a honeycomb lattice quantum *XY* magnet CoTiO$_3$. *Phys. Rev. X* **10**, 011062 (2020).
17. Elliot, M. et al. Order-by-disorder from bond-dependent exchange and intensity signature of nodal quasiparticles in a honeycomb cobaltate. *Nat. Commun.* **12**, 1–7 (2021).
18. Dubrovin, R. et al. Lattice dynamics and spontaneous magnetodielectric effect in ilmenite CoTiO$_3$. *J. Alloys Compd.* **858**, 157633 (2021).
19. Lockwood, D. & Cottam, M. Light scattering from magnons in MnF$_2$. *Phys. Rev. B* **35**, 1973 (1987).
20. Fleury, P. & Loudon, R. Scattering of light by one- and two-magnon excitations. *Phys. Rev.* **166**, 514 (1968).
21. Yang, Y. et al. Signatures of non-Loudon-Fleury Raman scattering in the Kitaev magnet β-Li$_2$IrO$_3$. *Phys. Rev. B* **105**, L241101 (2022).
22. Cottam, M. Theory of two-magnon raman scattering in antiferromagnets at finite temperatures. *J. Phys. C: Solid State Phys.* **5**, 1461 (1972).
23. Liu, Q. et al. Magnetic order in xy-type antiferromagnetic monolayer cops 3 revealed by Raman spectroscopy. *Phys. Rev. B* **103**, 235411 (2021).
24. Scagliotti, M., Jouanne, M., Balkanski, M., Ouvrard, G. & Benedek, G. Raman scattering in antiferromagnetic feps 3 and fepse 3 crystals. *Phys. Rev. B* **35**, 7097 (1987).
25. Balkanski, M., Wallis, R. F. & Haro, E. Anharmonic effects in light scattering due to optical phonons in silicon. *Phys. Rev. B* **28**, 1928–1934 (1983).
26. Dietz, R., Parisot, G. & Meixner, A. Infrared absorption and Raman scattering by two-magnon processes in NiO. *Phys. Rev. B* **4**, 2302 (1971).
27. Tanabe, Y. et al. Direct optical excitation of two and three magnons in α-Fe$_2$O$_3$. *Low Temp. Phys.* **31**, 780–785 (2005).
28. Lujan, D. et al. Magnons and magnetic fluctuations in atomically thin MnBi$_2$Te$_4$. *Nat. Commun.* **13**, 1–7 (2022).
29. Rosenblum, S., Francis, A. H. & Merlin, R. Two-magnon light scattering in the layered antiferromagnet NiPS$_3$: Spin-1/2-like anomalies in a spin-1 system. *Phys. Rev. B* **49**, 4352–4355 (1994).
30. Knoll, P., Thomsen, C., Cardona, M. & Murugaraj, P. Temperature-dependent lifetime of spin excitations in RBa2Cu3O6 (R = *Eu, Y*). *Phys. Rev. B Codens Mater.* **42**, 4842–4845 (1990).
31. Sandilands, L. J., Tian, Y., Plumb, K. W., Kim, Y.-J. & Burch, K. S. Scattering continuum and possible fractionalized excitations in RuCl$_3$. *Phys. Rev. Lett.* **114**, 147201 (2015).
32. Mai, T. T. et al. Magnon-phonon hybridization in 2d antiferromagnet MnPSe$_3$. *Sci. Adv.* **7**, eabj3106 (2021).
33. Arruabarrena, M., Leonardo, A., Rodriguez-Vega, M., Fiete, G. A. & Ayuela, A. Out-of-plane magnetic anisotropy in bulk ilmenite CoTiO$_3$. *Phys. Rev. B* **105**, 144425 (2022).
34. Rezende, S. & White, R. Multimagnon theory of antiferromagnetic resonance relaxation. *Phys. Rev. B* **14**, 2939 (1976).
35. Kopietz, P. Magnon damping in the two-dimensional quantum heisenberg antiferromagnet at short wavelengths. *Phys. Rev. B* **41**, 9228 (1990).
36. Nikitin, S. E. et al. Thermal evolution of Dirac magnons in the honeycomb ferromagnet CrBr3. *Phys. Rev. Lett.* **129**, 127201 (2022).
37. Cottam, M. Spin-phonon interactions in a Heisenberg antiferromagnet. ii. the phonon spectrum and spin-lattice relaxation rate. *J. Phys C Solid State Phys.* **7**, 2919 (1974).
38. Rezende, S. M., Rodríguez-Suárez, R. L. & Azevedo, A. Diffusive magnonic spin transport in antiferromagnetic insulators. *Phys. Rev. B* **93**, 054412 (2016).
39. Yuan, B. et al. Field-dependent magnons in the honeycomb antiferromagnet cotio 3. *Phys. Rev. B* **109**, 174440 (2024).
40. Li, Y. et al. Ring-exchange interaction effects on magnons in the Dirac magnet cotio 3. *Phys. Rev. B* **109**, 184436 (2024).
41. Choe, J. et al. Magnetoelastic coupling driven magnon gap in a honeycomb antiferromagnet. *Phys. Rev. B* **110**, 104419 (2024).
42. Zhitomirsky, M. E. & Chernyshev, A. L. Colloquium: spontaneous magnon decays. *Rev. Mod. Phys.* **85**, 219–242 (2013).
43. Maksimov, P. A. & Chernyshev, A. L. Field-induced dynamical properties of the *XXZ* model on a honeycomb lattice. *Phys. Rev. B* **93**, 014418 (2016).
44. Do, S.-H. et al. Gaps in topological magnon spectra: intrinsic versus extrinsic effects. *Phys. Rev. B* **106**, L060408 (2022).
45. Cai, Z. et al. Topological magnon insulator spin excitations in the two-dimensional ferromagnet CrBr$_3$. *Phys. Rev. B* **104**, L020402 (2021).
46. Zhu, F. et al. Topological magnon insulators in two-dimensional van der waals ferromagnets CrSiTe$_3$ and CrGeTe$_3$: Toward intrinsic gap-tunability. *Sci. Adv.* **7**, eabi7532 (2021).
47. Lee, K. H., Chung, S. B., Park, K. & Park, J.-G. Magnonic quantum spin hall state in the zigzag and stripe phases of the antiferromagnetic honeycomb lattice. *Phys. Rev. B* **97**, 180401 (2018).
48. Bazazzadeh, N. et al. Magnetoelastic coupling enabled tunability of magnon spin current generation in two-dimensional antiferromagnets. *Phys. Rev. B* **104**, L180402 (2021).
49. Karaki, M. J. et al. An efficient material search for room-temperature topological magnons. *Sci. Adv.* **9**, eade7731 (2023).
50. Colpa, J. Diagonalization of the quadratic boson hamiltonian. *Phys. A: Stat. Mech. App.* **93**, 327 – 353 (1978).
51. Harris, A. B., Kumar, D., Halperin, B. I. & Hohenberg, P. C. Dynamics of an antiferromagnet at low temperatures: spin-wave damping and hydrodynamics. *Phys. Rev. B* **3**, 961–1024 (1971).
52. Anderson, P. W. *Basic Notions of Condensed Matter Physics* (Menlo Park, 1984).
53. Bayrakci, S. P. et al. Lifetimes of antiferromagnetic magnons in two and three dimensions: experiment, theory, and numerics. *Phys. Rev. Lett.* **111**, 017204 (2013).
54. Chen, L. et al. Magnetic field effect on topological spin excitations in CrI3. *Phys. Rev. X* **11**, 031047 (2021).

Author contributions

J.H. and J.Z. grew the CTO bulk crystals and characterized the samples. J.C., D.L., G.Y., and C.N. performed magneto-Raman measurements under the supervision of R.H. and X.L. Data were analyzed by J.C., D.L., F.Y.G., T.N.N., R.H., and X.L. The model calculations are performed by M.R.V., J.C., B.M., A.L., M.A., and A.A. J.C., G.F., M.R.V., R.H., and X.L. wrote the paper with the input from all authors.

Competing interests

The authors declare no competing interests.

Additional information

Supplementary information The online version contains supplementary material available at https://doi.org/10.1038/s41467-025-60287-2.

Correspondence and requests for materials should be addressed to Martin Rodriguez-Vega, Rui He or Xiaoqin Li.

Peer review information *Nature Communications* thanks the anonymous, reviewers for their contribution to the peer review of this work. A peer review file is available.

Reprints and permissions information is available at http://www.nature.com/reprints

Publisher's note Springer Nature remains neutral with regard to jurisdictional claims in published maps and institutional affiliations.